1   **Multimodal Integration of Alzheimer's Plasma Biomarkers, MRI,**

2   **and Genetic Risk for Individual Prediction of Cerebral Amyloid**

3   **Burden**

4

5   Yichen Wang[1,2,3#], Lairai H.J. Chen[1,2,3#], Yuxin Cheng[4], Yuyan Cheng[5], Shiyun Zhao[5],

6   Yidong Jiang[1], Tianyu Bai[1,2,3], Yanxi Huo[1,2,3], Kexin Wang[1,2,3], Mingkai Zhang[6], Weijie

7   Huang[7], Guozheng Feng[8], Ying Han[6,9,10,11,12,13]*, Ni Shu[1,2,3]*

8

9   [1]State Key Laboratory of Cognitive Neuroscience and Learning & IDG/McGovern

10   Institute for Brain Research, Beijing Normal University, Beijing, China

11   [2]BABRI Centre, Beijing Normal University, Beijing, China

12   [3]Beijing Key Laboratory of Brain Imaging and Connectomics, Beijing Normal University,

13   Beijing, China

14   [4]State Key Laboratory of Oil and Gas Reservoir Geology and Exploitation, Southwest

15   Petroleum University, Chengdu, 610500, Sichuan, P. R. China

16   [5]School of Mathematical Sciences, Beijing Normal University, Beijing, China

17   [6]Department of Neurology, XuanWu Hospital of Capital Medical University, Beijing,

18   China

19   [7]College of Artificial Intelligence, Nanjing University of Aeronautics and Astronautics,

20   MOE Key Laboratory of Brain Computer Intelligence Technology, Nanjing 211106,

21   China

1   [8]Tri-Institutional Center for Translational Research in Neuroimaging and Data Science

2   (TReNDS), Atlanta, GA, USA

3   [9]School of Biomedical Engineering, Hainan University, Haikou 570228, China

4   [10]Center of Alzheimer's Disease, Beijing Institute for Brain Disorders, Beijing 100053,

5   China

6   [11]National Clinical Research Center for Geriatric Diseases, Beijing 100053, China

7   [12]The Central Hospital of Karamay, Xinjiang 834000, China

8   [13]Institute of Biomedical Engineering, Shenzhen Bay Laboratory, Shenzhen 518132,

9   China

10   Yichen Wang and Lairai H.J. Chen contributed equally to this work.

11   **Corresponding author**

12   *Ni Shu, Email: nshu@bnu.edu.cn, No. 19, Xinjiekouwai St, Haidian District, Beijing,

13   100875, P. R. China

14   *Han Ying, Email: hanying@xwh.ccmu.edu.cn, XuanWu Hospital of Capital Medical

15   32 University, Beijing, 100053, China

16   **ORCID**

17   Yichen Wang: https://orcid.org/0009-0006-4283-7986

18   Lairai H.J. Chen: https://orcid.org/0000-0002-4362-1056

19   Yuxin Cheng: https://orcid.org/0009-0008-7684-0723

20   Yuyan Cheng: https://orcid.org/0009-0000-1355-7383

21   Shiyun Zhao: https://orcid.org/0009-0008-3816-1367

1   Yidong Jiang: https://orcid.org/0009-0005-4406-9549

2   Tianyu Bai: https://orcid.org/0009-0002-9357-5497

3   Yanxi Huo: https://orcid.org/0009-0002-8448-3275

4   Mingkai Zhang: https://orcid.org/0009-0001-9846-123X

5   Weijie Huang: https://orcid.org/0000-0002-2481-1188

6   Guozheng Feng: https://orcid.org/0000-0002-6937-8592

7   Han Ying: https://orcid.org/0000-0003-0377-7424

8   Ni Shu: https://orcid.org/0000-0003-2420-2910

9

Abstract

2   Alzheimer's disease (AD), the most prevalent neurodegenerative disorder, is marked by

3   the accumulation of amyloid-β (Aβ) plaques. Although cerebral Aβ positron emission

4   tomography (Aβ-PET) remains the gold standard for assessing cerebral Aβ burden, its

5   clinical utility is hindered by cost, radiation exposure, and limited availability. Plasma

6   biomarkers serve as promising non-invasive predictors of cerebral Aβ burden, but reliance

7   on a single marker often leads to suboptimal predictive performance. To address this, we

8   proposed a multimodal machine learning strategy that integrates readily accessible and

9   non-invasive features—such as plasma biomarkers, structural magnetic resonance imaging

10   (sMRI)-derived atrophy measures, diffusion tensor imaging (DTI)-based structural

11   connectomes (SCs), and genetic risk profiles—to predict cerebral Aβ burden and evaluate

12   the relative contribution of each modality to predictive performance. Specifically, a

13   random forest regressor was trained using data from the Alzheimer's Disease

14   Neuroimaging Initiative (ADNI; n = 150) and evaluated with leave-one-out

15   cross-validation. Our results showed that integrating multimodal features improves the

16   predictive power on cerebral amyloid burden: while the baseline model using plasma and

17   clinical variables alone achieved an R^2 of 0.52, adding neuroimaging and apolipoprotein E

18   (APOE) genotype features improved performance ($R^2 = 0.617$), and replacing APOE with

19   polygenic risk scores (PRS) further enhanced accuracy ($R^2 = 0.637$). The predictive value

20   of multimodal integration was also replicated in an independent cohort (SILCODE; n =

21   101). Moreover, a multiclass classifier trained with the same multimodal features achieved

22   high accuracy in distinguishing clinical stages of Aβ burden—normal controls (NC), mild

23   cognitive impairment (MCI), and Alzheimer's disease (AD)—with area under the curve

24   (AUC) values of 0.86, 0.77, and 0.93, respectively. These findings highlight the value of

25   combining plasma, imaging, and genetic data to non-invasively estimate cerebral Aβ

26   burden, offering a potential alternative to PET imaging for early AD risk assessment.

1   **Keyword**: Alzheimer's disease; Amyloid-β burden; Plasma biomarkers; Structural MRI;

2   Structural connectome; Polygenic risk score; APOE ε4 genotype; Multimodal machine

3   learning

4

1

1 Introduction

Alzheimer's disease (AD) is the most prevalent neurodegenerative disorder, characterized by the accumulation of amyloid-β (Aβ) plaques and neurofibrillary tangles, both of which are closely linked to cognitive decline[1,2]. Aβ positron emission tomography (Aβ-PET) remains the gold standard for in vivo quantification of cerebral Aβ burden, providing region-specific estimates of amyloid deposition[3]. However, its high cost, invasive nature, and limited accessibility hinder its applicability for large-scale or routine individual screening.

Plasma biomarkers—including phosphorylated tau (reflecting tau hyperphosphorylation), β-amyloid 42/40 ratio ($A\beta_{42}/A\beta_{40}$; indexing amyloid burden), neurofilament light chain (NfL; indicating axonal injury), and glial fibrillary acidic protein (GFAP; reflecting astrocytic activation)—have shown promise as accessible, non-invasive indicators for estimating cerebral Aβ burden[4]. However, their standalone predictive performance remains limited, particularly at the individual level, due to biological heterogeneity and the indirect nature of peripheral measurements. Structural MRI (sMRI) and diffusion tensor imaging (DTI) provide non-invasive insights into brain changes associated with Alzheimer's disease[5]. sMRI characterizes regional atrophy, whereas DTI-derived structural connectomes (SCs), capturing inter-regional white matter connectivity[6,7]. Genetic factors also modulate the predictive capacity of plasma biomarkers. The

1   apolipoprotein E (APOE) ε4 allele, the most established genetic risk factor for AD[8], is

2   easily genotyped and widely used in clinical settings. Polygenic risk scores (PRS),

3   although theoretically more comprehensive by aggregating genome-wide variants, are

4   often limited by their cost and complexity[9]. Both may provide complementary information

5   beyond plasma biomarkers[10,11]. However, given the higher cost of PRS assessment, it is

6   necessary to consider the feasibility of using APOE genotype as a cost-effective proxy.

7   Together, plasma, neuroimaging, and genetic biomarkers capture distinct yet

8   complementary dimensions of Alzheimer's disease pathophysiology[12]. However,

9   integrating these heterogeneous data sources remains challenging due to their different

10   dimensionality and complex interdependencies. Among machine learning approaches,

11   random forest (RF) algorithms are particularly well-suited for modeling multimodal

12   biomedical data[13]. RFs can effectively accommodate nonlinear relationships, and provide

13   interpretable feature importance metrics, making them ideal for individualized prediction

14   of cerebral Aβ burden.

15   Previous studies have explored Aβ burden prediction using selected data modalities, but

16   few have integrated multiple complementary biological domains, such as plasma, imaging,

17   and genetics. For example, Ramanan et al. demonstrated that adding genetic risk scores to

18   plasma biomarkers improved diagnostic accuracy for brain amyloidosis[10]. Santos et al

19   validated the utility of plasma biomarkers for predicting dementia conversion in a

20   Brazilian cohort[14]. Other studies have utilized machine learning on imaging and cognitive

1 features to identify incipient dementia cases[15], while some reviews have summarized

2 available plasma assays and highlighted their promise for clinical translation[16]. However,

3 these efforts typically focus on one or two modalities. A truly integrative multimodal

4 framework—combining plasma, neuroimaging, and genetic data—is still lacking.

5 Furthermore, no prior study has systematically evaluated the relative contribution of each

6 modality within a unified predictive framework, leaving it unclear which data sources

7 offer the most substantial incremental value.

8 To address these gaps, we proposed a multimodal machine learning framework based on

9 ML to predict continuous cerebral Aβ burden. Specifically:

10 (1) We evaluated the model using data from the ADNI, systematically examining the

11 added predictive value of structural MRI, DTI-derived structural connectomes, and genetic

12 features beyond plasma biomarkers; (2) We compared the predictive performance of

13 APOE genotype and PRS within this framework to evaluate their respective utility. (3) We

14 validated the model in an independent Chinese cohort (SILCODE) to assess cross-cohort

15 generalizability

2　Methods

2.1 Participants and Study Design

18 This study conducted a secondary analysis using publicly available data from the ADNI, a

19 longitudinal project aimed at identifying early biomarkers of AD through multimodal data

1 collection. ADNI participants were included if they were aged 55–90 years, generally in

2 good health, fluent in English or Spanish, and had a Geriatric Depression Scale score

3 below 6. Clinical diagnoses—cognitively unimpaired (CU), mild cognitive impairment

4 (MCI), or AD—were determined according to standard ADNI criteria based on subjective

5 memory complaints, objective neuropsychological assessments, and clinician-rated global

6 functioning. To ensure multimodal data availability, participants with sMRI, DTI, genetic

7 data, plasma biomarkers, and Aβ-PET imaging acquired within a one-year interval were

8 selected from the ADNI-GO, ADNI-2, and ADNI-3 phases.

9 To assess the generalizability, we performed external validation using the SILCODE

10 cohort—a prospective multicenter study of AD and cognitive impairment in the mainland

11 Chinese population. SILCODE participants were included if they were aged 45–90 years,

12 right-handed, native Mandarin speakers, and had complete multimodal data for sMRI, DTI,

13 plasma biomarkers, APOE genotyping, and Aβ-PET imaging within a one-year window.

14 Demographic characteristics of both cohorts, stratified by diagnostic group, are

15 summarized in **Table 1**.

	ADNI			SILCODE		
Diagnose	CU	MCI	AD	CU	MCI	AD
N	97	43	10	57	24	20
Age	71.36±6.02	74.84±8.62	72.27±6.57	68.16±5.71	70.46±6.31	71.40±10.98
Female	36(37%)	26(60%)	7(70%)	40(61%)	14(42%)	12(60%)

Pet_CL	21.81±31.15	44.53±54.78	102.10±46.53	\	\	\
SUVR	\	\	\	1.03±0.11	1.09±0.16	1.3±0.17
Pla_tau217	0.21±0.27	0.34±0.34	0.73±0.38	\	\	\
Pla_tau181	\	\	\	2.04±0.94	2.82±1.04	3.79±1.17
Pla_Aβ42/Aβ40	0.09±0.01	0.13±0.2	0.08±0.01	0.06±0.02	0.06±0.01	0.05±0.02
Pla_NfLQ	19.56±8.7	23.24±12.84	25.58±8.55	17.64±7.1	22.09±7.71	31.62±22.82
Pla_GFAP	159.96±78.9	172.83±107.16	244.32±114.55	102.32±44.49	118.08±70.02	164.09±114.95
APOE_e4	0.41±0.63	0.65±0.65	1±0.67	0.23±0.46	0.5±0.59	0.55±0.51
PRS_1e-6	-0.16±0.94	0.12±0.89	0.25±0.62	\	\	\
Education	16.93±2.28	15.63±2.55	15.6±1.6	14.51±3.24	13.29±2.8	11.75±4.24
MMSE	29.24±1.17	26.63±2.9	23.4±2.17	28.42±1.7	24.54±2.38	18.35±6.39

Table 1 | Demographic, clinical, imaging, and biomarker characteristics of participants in the ADNI and SILCODE cohorts, stratified by diagnostic group: cognitively unimpaired (CU), mild cognitive impairment (MCI), and Alzheimer's disease (AD). Values are reported as mean ± standard deviation or N (%). PET_CL: Centiloid values from amyloid PET; SUVR: standardised uptake value ratio from amyloid PET; Pla_tau217 and Pla_tau181: plasma phosphorylated tau at threonine 217 and 181, respectively; Pla_Aβ42/Aβ40: plasma amyloid-β 42/40 ratio; Pla_NfLQ: plasma neurofilament light chain; Pla_GFAP: plasma glial fibrillary acidic protein; APOE_e4: apolipoprotein E ε4 dosage (range: 0–2); PRS_1e-6: polygenic risk score based on SNPs with $p < 1\times10^{-6}$; Education: years of formal education; MMSE: Mini-Mental State Examination score. "\" indicates variables not available in the corresponding cohort or subgroup.

2.2 MRI Data Acquisition

sMRI and DTI data were collected from both the ADNI and SILCODE cohorts. In ADNI, MRI scans were acquired using 3.0 Tesla (3T) scanners from Philips, Siemens, or GE

1 Healthcare across the ADNI-GO, ADNI-2, and ADNI-3 phases. For sMRI, a standardized

2 protocol was used, with typical parameters including a repetition time (TR) of 6.7 ms,

3 echo time (TE) of 3.1 ms, flip angle of 9°, field of view (FOV) of 256 × 256 × 170 mm³,

4 slice thickness of 1.2 mm, and voxel size of 1.0–1.11 mm³, covering 170 sagittal slices.

5 DTI scans in ADNI-GO and ADNI-2 were acquired using GE 3T scanners with TR =

6 9000 ms, TE = 60–70 ms, and voxel size = 1.37 × 1.37 × 2.7 mm³. Each scan included 30

7 diffusion-weighted directions (b = 1000 s/mm²) and 5 non-diffusion-weighted (b = 0)

8 images. For ADNI-3, an updated protocol was used with a resolution of 2 × 2 × 2 mm³,

9 TR = 7200 ms, TE = 56 ms, 35 axial slices, and a total scan time of approximately 7.5

10 minutes.

11 In the SILCODE cohort, imaging was performed using a 3T integrated PET/MR scanner

12 (SIGNA PET/MR, GE Healthcare) at Xuanwu Hospital, Capital Medical University.

13 sMRI was acquired using a gradient-recalled echo sequence with TR = 2300 ms, inversion

14 time (TI) = 900 ms, TE = 2.26 ms, flip angle = 8°, FOV = 256 × 256 mm², slice thickness

15 = 1 mm, and isotropic voxel size of 1 mm³. DTI data were collected using a spin-echo

16 echo-planar imaging (EPI) sequence with TR = 4500 ms, TE = 65 ms, voxel size = 2 × 2 ×

17 2 mm³, and 64 slices. Diffusion gradients were applied in 128 directions, including 64 at b

18 = 1000 s/mm² and 64 at b = 2000 s/mm², along with one non-diffusion-weighted (b = 0)

19 image.

2.3 MRI Data Processing

All imaging data were preprocessed using standardized protocols adapted from the UK Biobank pipeline[17], implemented using *FSL*[18], *FreeSurfer*[19], and *MRtrix3*[20]. Raw DICOM images were converted to NIfTI format using *dcm2niix*[21]. For diffusion imaging, b-value distributions were inspected prior to preprocessing. sMRI preprocessing for both cohorts included skull stripping and bias field correction using FSL, followed by cortical reconstruction and volumetric segmentation using FreeSurfer v6.0. This yielded native-space parcellations based on the Desikan–Killiany atlas. These parcellations were further used to extract mean SUVR values within regions of interest (ROIs) for each participant. DTI data were corrected for head motion, eddy currents, and EPI distortions using FSL's eddy[22].

SCs were constructed using a unified tractography pipeline. Fiber orientation distributions were estimated using constrained spherical deconvolution, followed by probabilistic tractography[23]. Tractography was seeded from the gray–white matter interface using the *5ttgmwmi* algorithm[24]. Brain network nodes were defined using a hybrid atlas comprising 100 cortical regions from the Schaefer atlas[25] and 16 subcortical regions from the Melbourne Subcortex Atlas (MSA) [26]. The resulting SC matrices were used for feature extraction and predictive modeling. To further characterize topological changes at the network level, we grouped the 116 regions into 8 functional modules based on Yeo's 7-network parcellation scheme and the MSA-defined subcortical network. The Yeo-7

11

1   system defines seven large-scale cortical functional networks: visual, somatomotor,

2   default mode, dorsal attention, salience/ventral attention, executive control and limbic

3   networks. The eighth module, subcortical, includes 16 subcortical nuclei defined by the

4   MSA.

5   ## 2.4 Quantification and Harmonization of Amyloid PET Measures

6   In the ADNI cohort, Aβ burden was quantified using Centiloid (CL) values [27,28], processed

7   uniformly by the University of California, Berkeley, and publicly released alongside the

8   official dataset. CL values were derived from cortex-wide $SUMMARY\_SUVR$ measures,

9   normalized to the whole cerebellum, and converted using tracer-specific formulas:

10   For [¹⁸F]-florbetapir (FBP):

$$CL = 188.22 \text{ x } SUMMARY\_SUVR - 189.16$$

11   For [¹⁸F]-florbetaben (FBB):

$$CL = 157.15 \times SUMMARY\_SUVR - 151.87$$

12    $SUMMARY\_SUVR$ values were based on sMRI-guided segmentation of four cortical

13   regions (frontal, cingulate, parietal, and temporal), with normalization to the whole

14   cerebellum; regional definitions are detailed in the Supplementary Materials (Table S1). In

15   ADNI cohort, we utilized the standardized CL values provided by ADNI rather than

16   recalculating SUVRs. This decision was based on two considerations: (i) the CL

17   framework enables cross-tracer and cross-scanner harmonization, improving

1   comparability and robustness; and (ii) the official CL pipeline has been extensively

2   validated and widely adopted, ensuring high reproducibility.

3   In the SILCODE cohort, Aβ PET imaging was conducted using the radiotracer

4   [^{18}F]-florbetapir (AV-45). Participants received an intravenous injection of 7 to 10 mCi of

5   [^{18}F]-florbetapir, followed by a rest period of approximately 40 min, after which a

6   20-minute static PET scan was performed. PET data acquisition employed a time-of-flight

7   ordered subset expectation maximization (TOF-OSEM) algorithm[29,30] with 8 iterations, a

8   field of view of 350×350 mm2, subset matrices of 32 at 192×192, and a full width at

9   half maximum (FWHM) of 3 mm. Aβ burden was quantified using $SUMMARY\_SUVR$

10   values, calculated with the same cortical and reference regions as in the ADNI processing
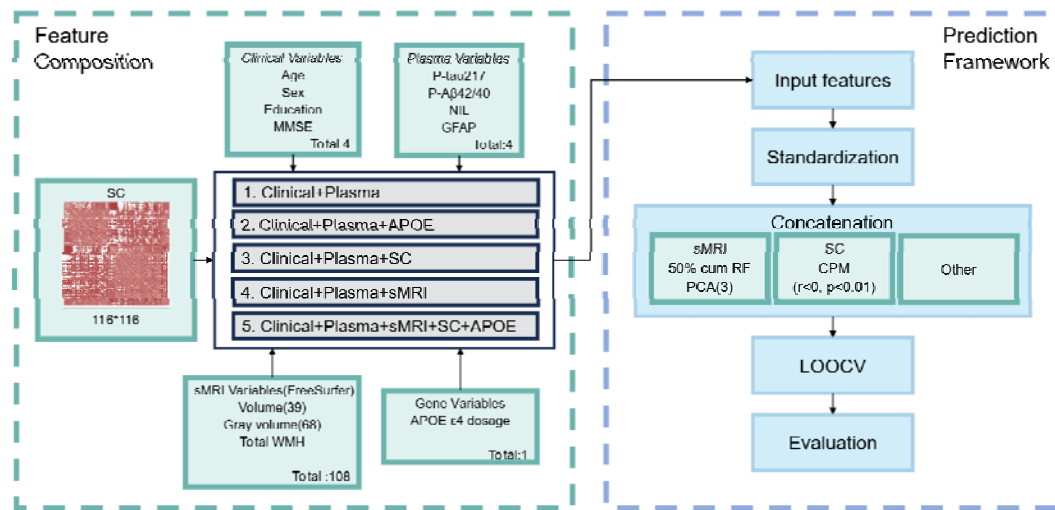
11   pipeline.

12   2.5 Genetic Risk Assessment

13   In ADNI, genotyping was performed using either the Illumina HumanOmniExpress or

14   Infinium Global Screening Array v2. Each dataset underwent separate preprocessing,

15   imputation, and quality control (QC) steps to ensure batch consistency. Preprocessing

16   involved recoding chromosome labels, removing non-autosomal variants and duplicate

17   SNPs, and correcting strand orientations using PLINK[31] and Bcftools[32]. Phasing used the

18   1000 Genomes Phase 3 panel[33], with imputation via Impute5[34]. Variants with imputation

19   INFO scores < 0.8 were excluded. After merging batches, unified QC removed SNPs with

20   minor allele frequency < 0.01, genotype missingness > 1%, or significant deviation from

1   Hardy–Weinberg equilibrium ($p < 1\times10^{-6}$). Individuals were excluded for high genotype

2   missingness, excessive heterozygosity (F-statistic ±3 SD), cryptic relatedness

3   (identity-by-descent > 0.125), or discrepancies between genetically inferred and reported

4   sex. PRS were computed using clumping and thresholding (C+T) based on AD GWAS

5   summary statistics[35], testing multiple p-value inclusion thresholds ($p < 10^{-6}$) combined

6   with LD-based clumping (window size=250 kb, $r^2<0.01$). Resulting scores were

7   standardized (Z-scores) for analysis. To control population stratification, the top five

8   genetic principal components derived via PCA were included as covariates. In SILCODE,

9   genome-wide genotyping was unavailable. Only APOE genotype data obtained through

10 standardized laboratory protocols were included as categorical covariates ($\varepsilon2$, $\varepsilon3$, $\varepsilon4$) in

11 analyses.

12 2.6 Multimodal Feature Integration and Predictive Modeling

13 To build an accurate prediction model and assess the added predictive value of sMRI, SC,

14 and genetic features beyond plasma biomarkers, we implemented a modular machine

15 learning framework enabling multimodal integration and systematic comparison across

16 feature combinations[10,11,36]. Taking plasma features as the baseline, we defined and

17 compared five feature combinations: Clinical + Plasma, Clinical + Plasma + APOE,

18 Clinical + Plasma + SC, Clinical + Plasma + MRI, and Clinical + Plasma + MRI + SC +

19 APOE. Two regression algorithms, linear regression and random forest (RF) regression,

20 were used for model benchmarking (Fig. 1).

1

Figure 1 | Multimodal machine learning framework for predicting cerebral amyloid-β burden.

An integrative pipeline was constructed to combine clinical, plasma, genetic, sMRI, and SC features. Five feature

combinations were tested under a LOOCV framework. sMRI features and SC were dimensionally reduced or selected

based on established criteria. Models were trained using both linear and random forest regressors.

Abbreviations: Aβ, amyloid-β; APOE, apolipoprotein E4 dosage; CPM, connectome-based predictive modeling; DTI,

diffusion tensor imaging; LOOCV, leave-one-out cross-validation; PCA, principal component analysis; PRS, polygenic

risk score; SC, structural connectome; sMRI, structural MRI; MMSE, Mini-Mental State Examination.

A total of 108 sMRI features were included, encompassing cortical volumes, surface areas,

and white matter hyperintensities (WMHs), all normalized by intracranial volume (ICV)

to control for inter-individual differences in brain size[37]. Within each training set, features

were ranked by importance using RF regression, with the top 50% retained and further

reduced to three orthogonal components using PCA. The SC features were extracted using

the CPM (connectome-based predictive modeling) approach[38,39]. For each training fold,

edges negatively correlated with CL values (Pearson's $r < 0$, $p < 0.01$) were identified.

1   The average strength of these negatively correlated edges was computed as a summary

2   feature per subject.

3   Model training and validation were performed using leave-one-out cross-validation

4   (LOOCV)[40]. All preprocessing, feature selection, and dimensionality reduction steps were

5   strictly confined to the training data in each fold. The resulting model was then applied to

6   the held-out subject to obtain unbiased performance estimates. The ML framework

7   modelling was conducted separately within ADNI and SILCODE.

8   To further evaluate model performance in classifying clinical Aβ burden status, we trained

9   multi-class Random Forest classifiers using sing clinical diagnosis labels (NC, MCI, AD)

10   as outcomes. Classification was conducted in ADNI cohort under the same LOOCV

11   framework, and model performance was assessed using area under the receiver operating

12   characteristic curve (AUC) for each class, as well as macro-average AUC to evaluate

13   overall discriminative ability. The same feature extraction and selection pipeline was

14   applied as in the regression setting, ensuring consistent input modalities across tasks.

15   2.7 Interpretability Analysis

16   To further elucidate the contributions of individual features to model predictions and

17   enhance interpretability, we employed SHapley Additive exPlanations (SHAP)[41] to

18   interpret the predictive power of each feature. SHAP quantifies the marginal contribution

19   of each input feature to a given prediction while accounting for feature interactions by

1   constructing a local linear model to approximate and interpret complex nonlinear models

2    $f(x)$, formulated as:

$$g(x') = \phi_0 + \sum_{i=1}^{M} \phi_i x'_i$$

3   where x' represents a simplified binany version of the input features (indicating feature

4   presence or absence), ϕ_0 denotes the expected output when all features are absent, and

5   ϕ_i represents the Shapley value of feature i, reflecting its marginal contribution to the

6   prediction.

7   ## 2.8 Sensitivity Analysis

8   To evaluate the robustness of the proposed framework, we conducted sensitivity analyses

9   across three methodological dimensions: (1) PRS construction, and (2) SC parcellation

10   templates

11   First, PRSs were reconstructed using clumping and thresholding with a range of p-value

12   cutoffs ($p < 10^{-5}$, 10^{-6} 10^{-7}, 10^{-8}, 10^{-9}, and 10^{-10}). Second, to evaluate the effect of brain

13   parcellation schemes, we derived SC features using an alternative atlas combining aparc

14   and MSA-16 (total 84 regions), replacing the default Schaefer-100 + MSA-16 template

15   (total 116 regions).

3 Results

3.1 Associations between features and cerebral amyloid-β burden
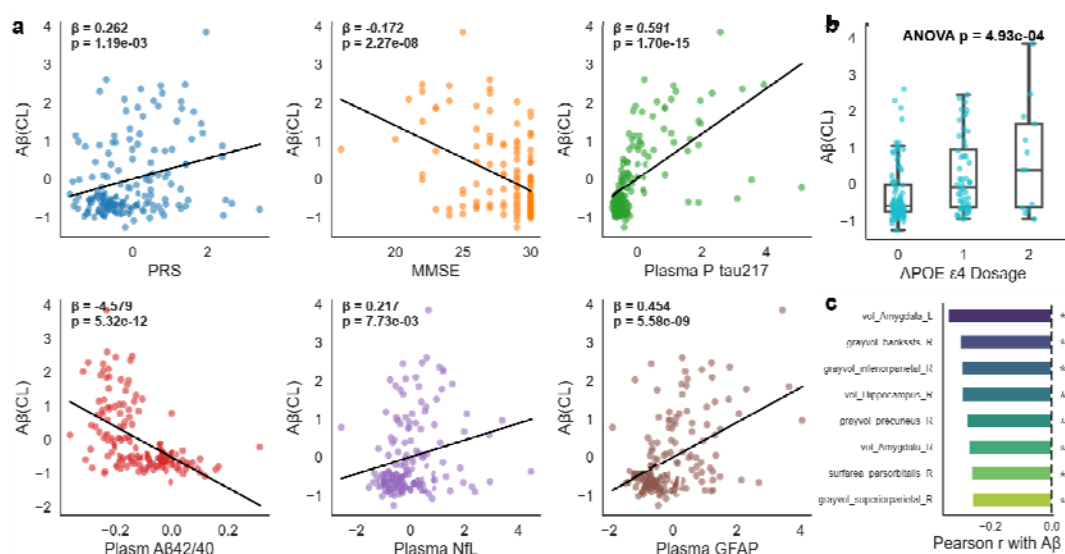

Figure 2 | Associations between plasma biomarkers, cognitive function, genetic risk, and brain structural features with standardized Aβ burden.

(a) Scatter plots showing the linear associations between Z-scored CL values and PRS, MMSE, p-tau$_{217}$, Aβ$_{42}$/Aβ$_{40}$ ratio, NfL, and GFAP. Standardized regression coefficients (β) and corresponding p-values are annotated in each panel.

(b) Boxplots illustrating the distribution of Z-scored CL values stratified by APOE ε4 allele dosage (0, 1, or 2 copies).

(c) The top eight ICV-normalized sMRI features (volume or surface area) most strongly correlated with Aβ burden, ranked by Pearson correlation coefficients. Asterisks (*) indicate significant associations (p < 0.05, uncorrected).

Abbreviations: Aβ, amyloid-β; APOE, apolipoprotein E; CL, Centiloid; GFAP, glial fibrillary acidic protein; MMSE, Mini-Mental state Examination; NfL, neurofilament light chain; PRS, polygenic risk score; ICV, Intracranial Volume; ANOVA, analysis of variance.

In the ADNI cohort, among plasma biomarkers, p-tau$_{217}$ showed the strongest positive association with cerebral Aβ burden (β = 0.591, p = 1.70×10^{-15}), followed by GFAP (β =

1   0.454, p = 5.58 × 10⁻□) and NfL ($\beta = 0.217$, p = 7.73 × 10⁻³). In contrast, the $A\beta_{42}/A\beta_{40}$

2   ratio was strongly and negatively associated with $A\beta$ burden ($\beta = -4.579$, p = 5.32 ×

3   10⁻¹²). Cognitive performance, as measured by MMSE, exhibited a modest negative

4   association with $A\beta$ burden ($\beta = -0.172$, p = 2.27 × 10⁻□), suggesting that amyloid

5   deposition contributes only partially to cognitive decline. Compared to plasma markers,

6   genetic features showed weaker associations: the PRS was positively correlated with $A\beta$

7   burden ($\beta = 0.262$, p = 1.19 × 10⁻³), while APOE ε4 dosage revealed a clear

8   dose-dependent increase in amyloid levels (Fig. 2a–b). Structural MRI analyses revealed

9   multiple brain regions associated with $A\beta$ burden. The eight regions with the strongest

10   correlations, as shown in Figure 2c, were mainly located in the medial temporal lobe (e.g.,

11   amygdala, hippocampus), parietal cortex (e.g., precuneus, inferior parietal lobule), and

12   subcortical areas. These spatial patterns are consistent with regions known to be

13   vulnerable in the early stages of Alzheimer's disease, reinforcing the link between

14   structural atrophy and amyloid deposition.

15

1 ## 3.2 Multimodal feature integration enhances Aβ burden prediction
2 ## performance

3

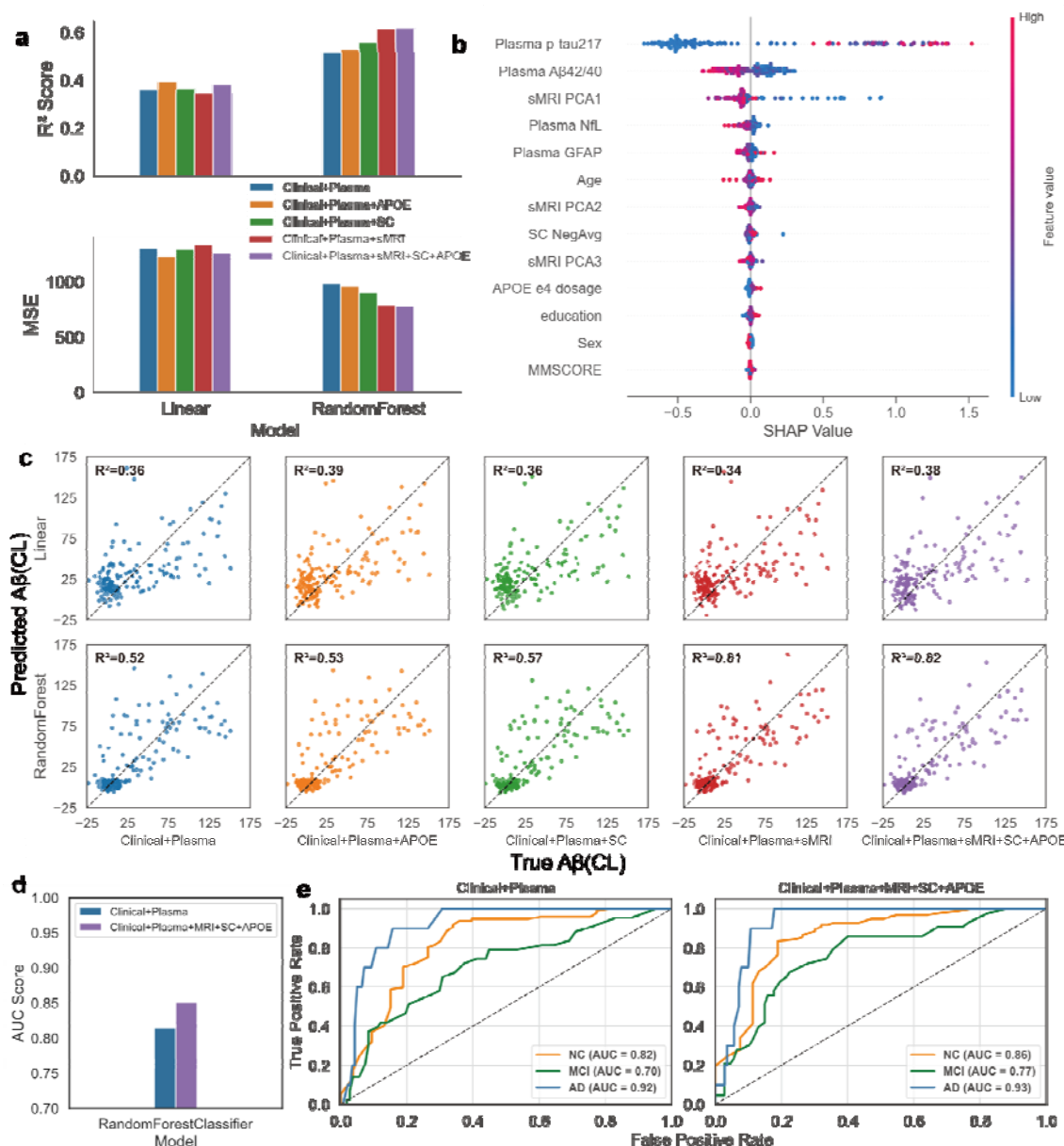4 Figure 3 | Model performance and SHAP-based feature importance for Aβ burden prediction in the ADNI cohort.

5 (a) R^2 and mean squared error (MSE) for linear regression (LR) and random forest (RF) models across different feature

6 combinations under leave-one-out cross-validation (LOOCV).

7 (b) SHAP summary plot showing the top features in the best-performing RF model (Clinical + Plasma + sMRI + SC +

8 APOE), ranked by mean absolute SHAP value. Each point represents a subject, with colour indicating feature value (red =

9 high, blue = low).

10 (c) Scatter plots of observed versus predicted Aβ burden (Centiloid values) for LR and RF models across all feature

11 combinations. R^2 values are shown for each model.

20

1 (d) Macro-average area under the receiver operating characteristic curve (AUC) for multi-class classification (NC, MCI,

2 AD) across different feature combinations using RF classifier.

3 (e) Class-specific AUC values for NC, MCI, and AD groups based on RF models trained with various combinations of

4 features.

5 Abbreviations: Aβ, amyloid-β; APOE, apolipoprotein E; GFAP, glial fibrillary acidic protein; MMSE, Mini-Mental State

6 Examination; NfL, neurofilament light chain; PCA, principal component analysis; SC, structural connectivity; SHAP,

7 SHapley Additive exPlanations; RF, random forest; LR, linear regression; MSE, mean squared error; ROC, receiver

8 operating characteristic; AUC, area under the curve; NC, cognitively normal; MCI, mild cognitive impairment; AD,

9 Alzheimer's disease; Clinical, demographic and cognitive measures.

10

11 We systematically evaluated the predictive performance of different feature combinations

12 under a LOOCV framework using data from the ADNI cohort. Linear regression showed

13 limited ability to model cerebral Aβ burden across all feature sets ($R^2 = 0.38$ for the

14 Clinical + Plasma + sMRI + SC + APOE model), indicating its inability to capture the

15 complex, nonlinear interactions inherent to multimodal data. In contrast, the RF model

16 consistently outperformed linear regression, with performance improving as more

17 modalities were integrated (Fig. 3a–b). Notably, the full model incorporating clinical

18 features, plasma biomarkers, sMRI, SC, and APOE genotype achieved the best predictive

19 accuracy ($R^2 = 0.617$) and lowest mean squared error (MSE = 770.1) (Fig. 3c),

20 highlighting the synergistic value of combining diverse biological information.

21 Specifically, the RF model using only clinical and plasma features achieved an R^2 of

22 0.515. Incremental gains were observed with the addition of APOE genotype ($R^2 = 0.527$),

23 SC features ($R^2 = 0.556$), and sMRI measures ($R^2 = 0.615$), with maximal performance

24 attained when all modalities were combined ($R^2 = 0.617$). Detailed R^2 and MSE metrics

25 for all feature sets are provided in Supplementary Table S2.

26 To interpret the model, we applied SHAP analysis to the best-performing RF model. The

27 most influential predictors were plasma biomarkers, particularly p-tau$_{217}$ and the Aβ$_{42}$/Aβ

28 $_{40}$ ratio, followed by principal components from sMRI, SC-derived connectivity metrics

29 and genetic feature. These results suggest that while plasma biomarkers offer strong

30 individual predictive power, imaging and genetic feature provide valuable complementary

31 information.

1 To assess classification performance across clinical stages, we further trained a multi-class

2 RF classifier using clinical diagnosis labels (NC, MCI, AD). Compared to the baseline

3 model using clinical and plasma features (AUC = 0.82 for NC, 0.70 for MCI, and 0.92 for

4 AD), the full multimodal model improved classification performance across all subgroups

5 (AUC = 0.86 for NC, 0.77 for MCI, and 0.93 for AD) (Fig. 3e). Macro-average AUC also

6 improved (Fig. 3d), reinforcing that multimodal integration enhances both continuous and

7 categorical prediction of cerebral amyloid pathology.

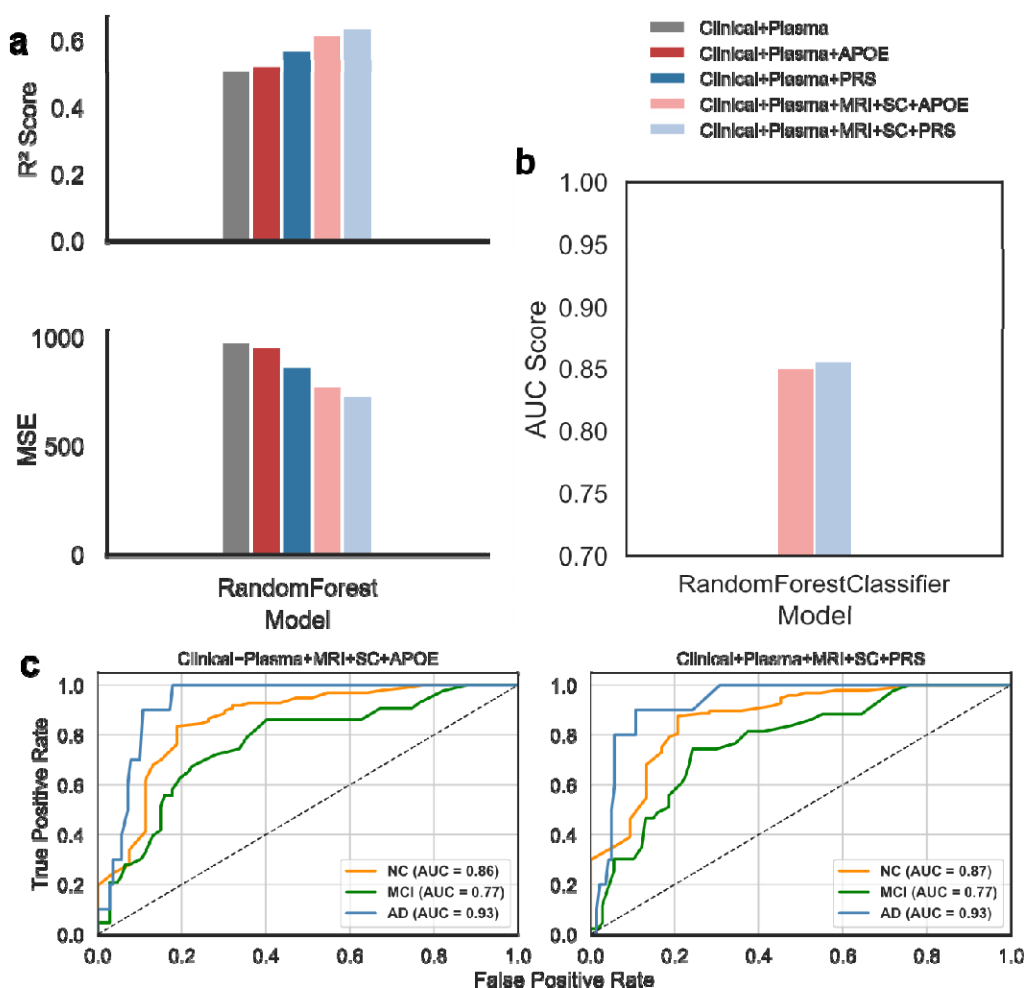8 3.3 Comparing the predictability of APOE and PRS

9

10

1   Figure 4 | Model performance with APOE or PRS for predicting Aβ burden in the ADNI cohort.

2   Bar plots display R^2 (top) and MSE (bottom) for models using different combinations of clinical, plasma, genetic, and

3   imaging features.

4   (b) AUC scores from multi-class Random Forest classifiers trained using CL-based Aβ labels (NC, MCI, AD) with either

5   APOE or PRS added to the baseline Clinical + Plasma + sMRI + SC model.

6   (c) ROC curves for each class (NC, MCI, AD) derived from models using APOE (left) or PRS (right) in the full feature

7   combination.

8   To evaluate the additive predictive value of genetic information, we compared the

9   performance of APOE genotype and PRS in predicting cerebral Aβ burden within the

10   ADNI cohort (Fig. 4). In the baseline model comprising clinical and plasma biomarkers,

11   the inclusion of APOE ε4 status led to a modest improvement in prediction accuracy (ΔR^2

12   = 0.012). In contrast, substituting APOE with PRS yielded a more substantial gain (ΔR^2 =

13   0.056), suggesting a broader capture of genetic risk beyond the APOE locus. A detailed

14   comparison is provided in Supplementary Materials (Table S3).

15   This advantage of PRS persisted when more complex models incorporating structural MRI

16   and structural connectivity features were used. Although the performance gap between

17   APOE and PRS narrowed in the full multimodal model (R^2_{APOE} = 0.617 vs. R^2_{PRS} = 0.637),

18   PRS consistently demonstrated higher predictive accuracy across all combinations.

19   This trend was also reflected in classification performance. As shown in Fig. 4b–c, both

20   APOE- and PRS-based models achieved similarly high AUCs in distinguishing between

21   NC, MCI, and AD groups based on CL-derived Aβ burden. The PRS-based model

22   achieved AUCs of 0.87 (NC), 0.77 (MCI), and 0.93 (AD), closely matching the

23   APOE-based model (0.86, 0.77, and 0.93, respectively). These results indicate that while

24   PRS provides superior continuous-level prediction of Aβ burden, its classification

25   performance is comparable to APOE when stratifying disease stages.

26

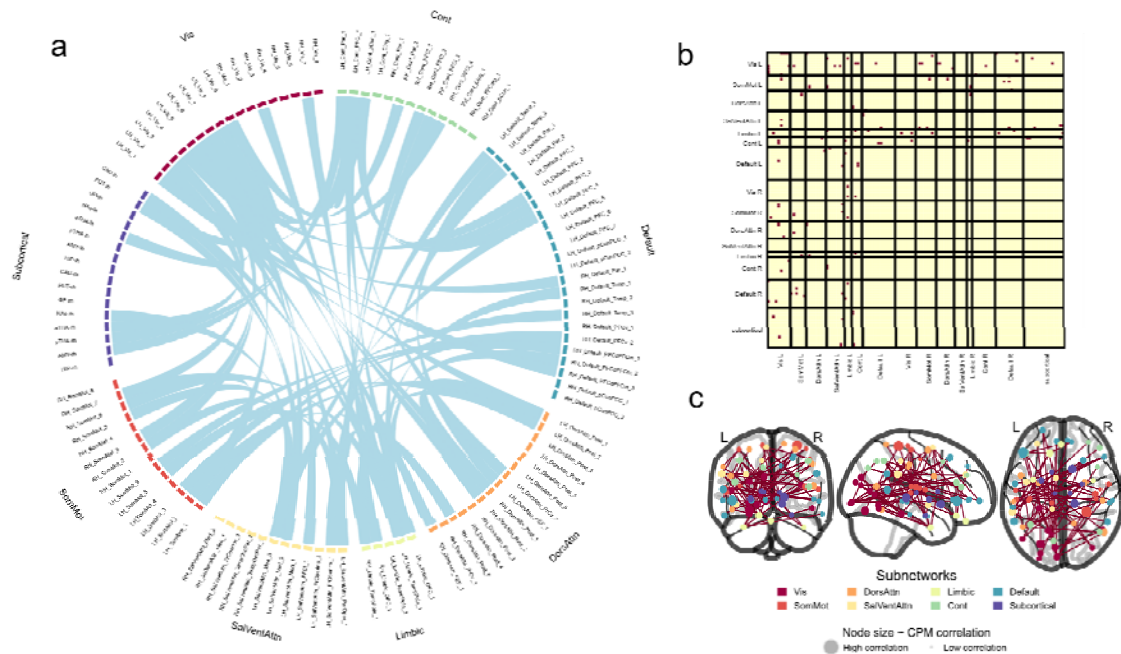1 ## 3.4 Distributed Network Disruption Associated with Aβ Burden

2
3 Figure 5 | Structural connections with common associations with CL value across all folds in ADNI.

4 (a) Chord diagram illustrating the intersection of significantly positive connections identified by CPM across all training

5 sets under the LOOCV framework. Nodes are grouped by functional subnetworks.

6 (b) Inter-subnetwork connectivity matrix displaying the distribution of stable connections among major functional

7 modules. Red dots indicate the presence of consistently selected edges; rows and columns represent different subnetworks.

8 (c) Cortical surface projection of stable structural connections. Node size indicates CPM correlation strength, and both

9 nodes and edges are colour-coded by functional subnetwork.

10 Abbreviations: CPM, connectome-based predictive modeling; LOOCV, leave-one-out cross-validation; Vis, visual

11 network; SomMot, somatomotor network; DorsAttn, dorsal attention network; SalVentAttn, salience/ventral attention

12 network; Limbic, limbic network; Default, default mode network; Cont, control network; Subcortical, subcortical

13 structures.

14 To identify SC consistently weakened by Aβ burden, we applied CPM under a LOOCV

15 framework. In each fold, connections negatively associated with CL values ($p < 0.01$)

16 were selected, and those recurring across all folds were retained, yielding 82 stable

17 disconnections (Fig. 5). To identify SC consistently weakened by Aβ burden, we applied

18 CPM under a LOOCV framework. In each fold, connections negatively associated with

1   CL values (p□<□0.01) were selected, and those recurring across all folds were retained,

2   yielding 82 stable disconnections (Fig. 5).

3   Among all functional subnetworks, the visual network exhibited the highest number of

4   disconnections, both within itself (n = 10) and in its connections with other

5   networks—particularly the control (n = 5), somatomotor (n = 4), and default mode (n = 4)

6   networks. This dominant pattern of disconnection suggests early vulnerability of

7   perceptual and attentional integration systems during amyloid accumulation.

8   In addition to the visual network, spatial mapping of affected regions revealed consistent

9   involvement of the medial prefrontal cortex and lateral parietal cortex—key hubs of the

10   default mode and frontoparietal control networks. These findings indicate that Aβ-related

11   disruptions extend beyond primary sensory systems and impact higher-order cognitive

12   networks implicated in early-stage AD.

13   Collectively, the observed disconnection patterns support a network-level framework for

14   understanding AD, wherein early amyloid deposition perturbs distributed integrative

15   systems. Structural connectome features derived from robust CPM analysis may thus

16   serve as sensitive and interpretable biomarkers for early disease characterization and risk

17   stratification.

18

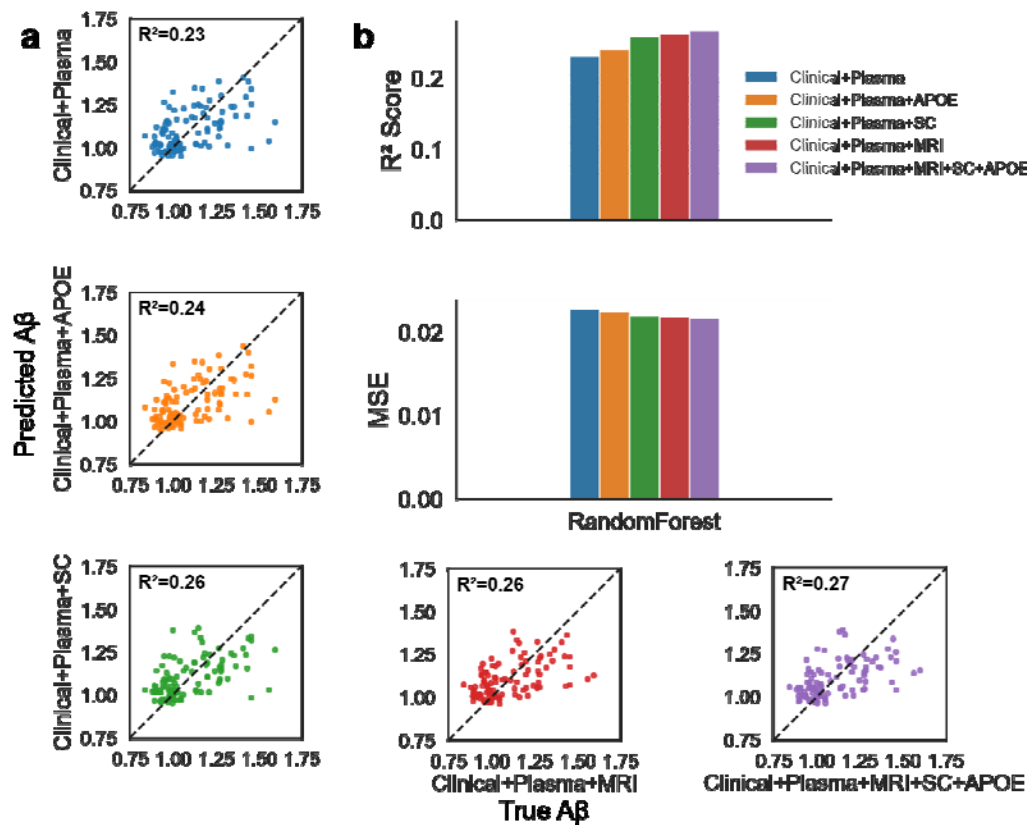1 ## 3.5 External validation in the SILCODE cohort

2

3 Figure 6 | Model performance for Aβ burden prediction in the SILCODE cohort.

4 (a) Scatter plots of observed vs. predicted Aβ SUVR values across five feature combinations using RF models. R² values

5 indicate model fit. The x-axis denotes observed SUVR values; the y-axis shows model-predicted values.

6 (b) Bar plots summarize model performance under a LOOCV framework. The upper panel shows R² values, and the lower

7 panel displays MSE across feature combinations.

8 Abbreviations: Aβ, amyloid-β; APOE, apolipoprotein E; GFAP, glial fibrillary acidic protein; MMSE, Mini-Mental State

9 Examination; NfL, neurofilament light chain; PCA, principal component analysis; SC, structural connectivity; RF, random

10 forest; MSE, mean squared error. Clinical, demographic and cognitive measures.

11

12 To assess generalizability, we performed external validation using the SILCODE cohort,

13 employing five feature combinations with RF models to predict Aβ PET SUVR (Fig. 6).

14 Relative to the baseline model (Clinical+Plasma; R²=0.232), incremental performance

1 improvements were observed upon adding APOE genotype (ΔR^2=+0.009), SC features

2 (ΔR^2=+0.027), and sMRI features (ΔR^2=+0.032). The full model

3 (Clinical+Plasma+MRI+SC+APOE) achieved the highest R^2 of 0.267, a detailed

4 comparison of R^2 and MSE across models is provided in Supplementary Materials (Table

5 S4). Although overall predictive accuracy was lower than in ADNI, the incremental

6 benefit pattern remained consistent, highlighting multimodal robustness. Lower

7 performance in SILCODE primarily reflected plasma biomarker differences: ADNI

8 utilized plasma p-tau$_{217}$, known for superior amyloid sensitivity, whereas SILCODE

9 employed the less sensitive but widely used p-tau$_{181}$. Prior studies have confirmed that

10 p-tau$_{217}$ better discriminates amyloid-positive individuals, partly explaining the observed

11 performance gap[42].

12 ## 3.6 Sensitivity Analysis

13 First, we tested multiple p-value thresholds ($p < 10^{-5}$ to 10^{-10}) for PRS construction using

14 the clumping-and-thresholding approach. All thresholds except $p < 10^{-5}$ improved

15 prediction over the plasma-only baseline, with the best performance observed at $p < 10^{-6}$.

16 These results underscore the importance of optimal thresholding for leveraging

17 genome-wide polygenic data (Table S5 and Fig S1). Second, we evaluated the impact of

18 different parcellation schemes on SC-based prediction. Alternative atlases with 84 and 116

19 regions both outperformed the baseline, with minor differences(Table S6 and Fig S2).

20 These findings suggest that SC features provide stable predictive value across anatomical

21 resolutions, with higher-resolution schemes offering more refined disease-relevant

1   connectivity patterns. Together, these analyses show that predictive gains from integrating

2   imaging and genetic features are robust to key modeling and design choices.

3   # 4   Discussion

4   We proposed a multimodal machine learning framework that integrates plasma

5   biomarkers, sMRI, DTI-derived structural connectivity (SC), and genetic risk to

6   non-invasively predict cerebral Aβ burden. In the ADNI cohort, adding sMRI, SC features,

7   and APOE genotype to clinical and plasma measures substantially improved model

8   performance ($R^2 = 0.617$ vs. $R^2 = 0.515$ for clinical + plasma only). Replacing APOE with

9   a genome-wide polygenic risk score (PRS) further enhanced predictive accuracy ($R^2 =$

10   0.637), highlighting the added value of capturing distributed genetic risk beyond the

11   APOE locus[10,35]. These results underscore the complementary strengths of different

12   modalities in characterizing early Alzheimer's disease pathology. External validation in

13   the SILCODE cohort supported the generalizability of our findings. Despite differences in

14   demographics, imaging protocols, and biomarker assays, consistent multimodal predictive

15   improvements across cohorts underscore the framework's generalizability and translational

16   potential.

17   Beyond continuous prediction, our multimodal model also showed improved classification

18   of individuals along the AD spectrum. Compared to the clinical + plasma model, the full

19   model achieved higher AUC scores across all diagnostic stages (NC: 0.86; MCI: 0.77; AD:

1   0.93), reinforcing its utility for both quantitative and categorical assessments of Aβ

2   burden.

3   Structurally, sMRI and SC features offered complementary insights into disease

4   mechanisms. While sMRI captured diffuse cortical atrophy, SC analysis revealed spatially

5   organized disconnection patterns. Notably, the visual network exhibited the highest

6   number of disrupted connections, both internally and with the control, somatomotor, and

7   default mode networks—suggesting early vulnerability of perceptual and integrative

8   attention systems in preclinical AD[25]. In addition, disconnections frequently involved the

9   medial prefrontal and lateral parietal cortices—core hubs of the default mode and

10   frontoparietal networks—coinciding with known regions of early Aβ deposition[43]. These

11   findings support a network-level interpretation of amyloid pathology and underscore the

12   utility of CPM-derived SC features as sensitive and interpretable markers of early brain

13   changes.

14   From a genetic perspective, APOE ε4 consistently demonstrated predictive utility across

15   cohorts. However, PRS outperformed APOE in the ADNI dataset, likely due to its

16   capacity to aggregate genome-wide susceptibility variants[10]. Despite its superior

17   predictive power, PRS remains less accessible and more costly, making APOE genotyping

18   a more pragmatic option in resource-limited clinical settings[8].

1. Sensitivity analyses confirmed that our findings were robust across different PRS p-value

2. thresholds and SC parcellation schemes. Nevertheless, several limitations warrant

3. consideration. First, our sample sizes were modest, which may restrict the generalizability

4. of the model to broader populations[44]. Second, the use of the Schaefer-100/MSA-16 atlas

5. prioritized interpretability but may have limited our ability to detect finer-grained network

6. effects[25]. Future work should explore higher-resolution or individualized parcellations to

7. refine SC modeling.

8. Implications. Collectively, our study demonstrates that integrating multimodal

9. information—including plasma biomarkers, neuroimaging, and genetic risk—can

10. significantly enhance non-invasive prediction of cerebral amyloid pathology. This scalable

11. framework holds potential for improving early AD risk stratification and may inform

12. future screening strategies in both clinical and population-based settings.

13.

References

15. 1.   Selkoe, D. J. & Hardy, J. The amyloid hypothesis of Alzheimer's disease at 25 years. *EMBO*
16. *Mol Med* **8**, 595–608 (2016).
17. 2.   DeTure, M. A. & Dickson, D. W. The neuropathological diagnosis of Alzheimer's disease.
18. *Molecular Neurodegeneration* **14**, 32 (2019).
19. 3.   Jack, C. R. *et al.* NIA-AA Research Framework: Toward a biological definition of
20. Alzheimer's disease. *Alzheimers Dement* **14**, 535–562 (2018).
21. 4.   Nakamura, A. *et al.* High performance plasma amyloid-β biomarkers for Alzheimer's disease.
22. *Nature* **554**, 249–254 (2018).

5. Zhang, M. *et al.* Relationship between topological efficiency of white matter structural connectome and plasma biomarkers across the Alzheimer's disease continuum. *Human Brain Mapping* **45**, e26566 (2024).

6. Racine, A. M. *et al.* Associations between white matter microstructure and amyloid burden in preclinical Alzheimer's disease: A multimodal imaging investigation. *NeuroImage: Clinical* **4**, 604–614 (2014).

7. Huang, W. *et al.* Individual Variability in the Structural Connectivity Architecture of the Human Brain. *J Neurosci* **45**, e2139232024 (2025).

8. Liu, C.-C., Liu, C.-C., Kanekiyo, T., Xu, H. & Bu, G. Apolipoprotein E and Alzheimer disease: risk, mechanisms and therapy. *Nat Rev Neurol* **9**, 106–118 (2013).

9. Leonenko, G. *et al.* Identifying individuals with high risk of Alzheimer's disease using polygenic risk scores. *Nat Commun* **12**, 4506 (2021).

10. Ramanan, V. K. *et al.* Genetic risk scores enhance the diagnostic value of plasma biomarkers of brain amyloidosis. *Brain* **146**, 4508–4519 (2023).

11. Karlsson, L. *et al.* Machine learning prediction of tau⬚PET in Alzheimer's disease using plasma, MRI, and clinical data.

12. Ying, Q. *et al.* Multi-Modal Data Analysis for Alzheimer's Disease Diagnosis: An Ensemble Model Using Imagery and Genetic Features. *Annu Int Conf IEEE Eng Med Biol Soc* **2021**, 3586–3591 (2021).

13. Sarica, A., Cerasa, A. & Quattrone, A. Random Forest Algorithm for the Classification of Neuroimaging Data in Alzheimer's Disease: A Systematic Review. *Front Aging Neurosci* **9**, 329 (2017).

14. Santos, L. E. *et al.* Performance of plasma biomarkers for diagnosis and prediction of dementia in a Brazilian cohort. *Nat Commun* **16**, 2911 (2025).

15. Identifying incipient dementia individuals using machine learning and amyloid imaging. *Neurobiology of Aging* **59**, 80–90 (2017).

16. Pais, M. V., Forlenza, O. V. & Diniz, B. S. Plasma Biomarkers of Alzheimer's Disease: A Review of Available Assays, Recent Developments, and Implications for Clinical Practice. *J Alzheimers Dis Rep* **7**, 355–380.

17. Alfaro-Almagro, F. *et al.* Image processing and Quality Control for the first 10,000 brain imaging datasets from UK Biobank. *NeuroImage* **166**, 400–424 (2018).

18. Jenkinson, M., Beckmann, C. F., Behrens, T. E., Woolrich, M. W. & Smith, S. M. FSL. *NeuroImage* **62**, 782–790 (2012).

19. Fischl, B. FreeSurfer. *NeuroImage* **62**, 774–781 (2012).

20. Tournier, J.-D. *et al.* MRtrix3: A fast, flexible and open software framework for medical image processing and visualization. *NeuroImage* **202**, 116137 (2019).

21. Li, X., Morgan, P. S., Ashburner, J., Smith, J. & Rorden, C. The first step for neuroimaging data analysis: DICOM to NIfTI conversion. *Journal of Neuroscience Methods* **264**, 47–56 (2016).

22. Andersson, J. L. R. & Sotiropoulos, S. N. An integrated approach to correction for off-resonance effects and subject movement in diffusion MR imaging. *Neuroimage* **125**, 1063–1078 (2016).

23. Tournier, J.-D., Calamante, F. & Connelly, A. Robust determination of the fibre orientation distribution in diffusion MRI: Non-negativity constrained super-resolved spherical deconvolution. *NeuroImage* **35**, 1459–1472 (2007).

24. Smith, R. E., Tournier, J.-D., Calamante, F. & Connelly, A. Anatomically-constrained tractography: Improved diffusion MRI streamlines tractography through effective use of anatomical information. *NeuroImage* **62**, 1924–1938 (2012).

25. Schaefer, A. *et al.* Local-global parcellation of the human cerebral cortex from intrinsic functional connectivity MRI. *Cerebral Cortex* **28**, 3095–3114 (2018).

26. Tian, Y., Margulies, D. S., Breakspear, M. & Zalesky, A. Hierarchical organization of the human subcortex unveiled with functional connectivity gradients. *Nature Neuroscience* **23**, 1421–1432 (2020).

27. Landau, S. M. *et al.* Amyloid deposition, hypometabolism, and longitudinal cognitive decline. *Annals of Neurology* **72**, 578–586 (2012).

28. Klunk, W. E. *et al.* The Centiloid Project: standardizing quantitative amyloid plaque estimation by PET. *Alzheimers Dement* **11**, 1-15.e1–4 (2015).

29. Chen, H.-J. *et al.* Amyloid pathology related to aberrant structure-function coupling of brain networks in Alzheimer's disease: insights from [18F]-florbetapir PET imaging. *Eur J Nucl Med Mol Imaging* (2025) doi:10.1007/s00259-025-07172-8.

30. Clark, C. M. *et al.* Use of florbetapir-PET for imaging beta-amyloid pathology. *JAMA* **305**, 275–283 (2011).

31. Purcell, S. *et al.* PLINK: a tool set for whole-genome association and population-based linkage analyses. *Am J Hum Genet* **81**, 559–575 (2007).

32. Danecek, P. *et al.* Twelve years of SAMtools and BCFtools. *Gigascience* **10**, giab008 (2021).

33. Auton, A. *et al.* A global reference for human genetic variation. *Nature* **526**, 68–74 (2015).

34. Rubinacci, S., Ribeiro, D. M., Hofmeister, R. J. & Delaneau, O. Efficient phasing and imputation of low-coverage sequencing data using large reference panels. *Nat Genet* **53**, 120–126 (2021).

35. Jansen, I. E. *et al.* Genome-wide meta-analysis identifies new loci and functional pathways influencing Alzheimer's disease risk. *Nat Genet* **51**, 404–413 (2019).

36. Prakash, R. S. *et al.* A whole-brain functional connectivity model of Alzheimer's disease pathology. *Alzheimers Dement* **21**, e14349 (2025).

37. Fjell, A. M. *et al.* One-year brain atrophy evident in healthy aging. *J Neurosci* **29**, 15223–15231 (2009).

38. Finn, E. S. Functional connectome fingerprinting: identifying individuals using patterns of brain connectivity. *nature NEUROSCIENCE* **18**, (2015).

39. Shen, X. *et al.* Using connectome-based predictive modeling to predict individual behavior from brain connectivity. *Nat Protoc* **12**, 506–518 (2017).

40. Varoquaux, G. Cross-validation failure: Small sample sizes lead to large error bars. *Neuroimage* **180**, 68–77 (2018).

41. Lundberg, S. M. & Lee, S.-I. A unified approach to interpreting model predictions. in *Advances in Neural Information Processing Systems* vol. 30 4765–4774 (2017).

42. Palmqvist, S. *et al.* Discriminative Accuracy of Plasma Phospho-tau217 for Alzheimer Disease vs Other Neurodegenerative Disorders. *JAMA* **324**, 772–781 (2020).

43. Thal, D. R., Rüb, U., Orantes, M. & Braak, H. Phases of Aβ-deposition in the human brain and its relevance for the development of AD. *Neurology* **58**, 1791–1800 (2002).

44. Luckett, E. S. *et al.* Association of Alzheimer's disease polygenic risk scores with amyloid accumulation in cognitively intact older adults. *Alzheimers Res Ther* **14**, 138 (2022).

Ethics declarations

All procedures performed in studies involving human participants were in accordance with the ethical standards of the institutional and/or national research committees and with the 1964 Declaration of Helsinki and its later amendments or comparable ethical standards.

For the ADNI cohort, ethical approval was obtained from the institutional review boards of all participating institutions (e.g., University of California, San Diego). For the SILCODE cohort, the study was approved by the Ethics Committee of Xuanwu Hospital, Capital Medical University. Written informed consent was obtained from all participants in both cohorts.

Consent for publication

Not applicable. No individual person's data is included in this study.

1 Data availability

2 The data used in this study are publicly available from the Alzheimer's Disease

3 Neuroimaging Initiative (ADNI; http://adni.loni.usc.edu) and the SILCODE data are

4 available upon reasonable request from the corresponding author.

5 Conflicts of Interest

6 The authors declare that they have no conflicts of interest regarding the publication of this

7 manuscript.

8

1

2

3

4

5

6